A Taylor series-based finite volume method for the Navier–Stokes equations

G. X. Wu[*,†] and Z. Z. Hu

Department of Mechanical Engineering, University College London, London WC1E 7JE, U.K.

SUMMARY

A Taylor series-based finite volume formulation has been developed to solve the Navier–Stokes equations. Within each cell, velocity and pressure are obtained from the Taylor expansion at its centre. The derivatives in the expansion are found by applying the Gauss theorem over the cell. The resultant integration over the faces of the cell is calculated from the value at the middle point of the face and its derivatives, which are further obtained from a higher order interpolation based on the values at the centres of two cells sharing this face. The terms up to second order in the velocity and the terms up to first order in pressure in the Taylor expansion are retained throughout the derivation. The test cases for channel flow, flow past a circular cylinder and flow in a collapsible channel have shown that the method is quite accurate and flexible. Copyright © 2008 John Wiley & Sons, Ltd.

1. INTRODUCTION

In the finite volume method (FVM), the computational domain is usually divided into many cells. It then integrates the governing equations over cells to obtain the discretized equations. For the Navier–Stokes (NS) equations, the integration of the convection term and the diffusion term within each cell is converted to that along its faces based on the Gauss theorem. Everything up to this stage is mathematically exact. Numerical error will, however, develop as the procedure moves forward.

There are several sources of error in FVM. The first one is that the variables are usually defined at the centre of each cell. Their values required on each face are obtained through interpolation

---

*Correspondence to: G. X. Wu, Department of Mechanical Engineering, University College London, London WC1E 7JE, U.K.
†E-mail: gx_wu@meng.ucl.ac.uk

from the centres of the two cells that share this face. For an unstructured mesh, the intersection G of the line linking the two centres with the face is usually not the middle point of the face, or there is the so-called skewness. Secondly the interpolation used to find the values at the face centre will itself introduce error. The third source of error occurs when the integration along the face is performed numerically.

In a recent work of Wu and Hu [1], the effect of the skewness was ignored. The face value at G is obtained through a linear interpolation and the integration along the face is calculated by multiplying the value at G with the area of the face. It can be shown in the present analysis below that the accuracy of this procedure is of order $O(h)$ for the convection term, where h is the typical element size of the mesh. What is more important, however, is that accuracy of the diffusion term is of order $O(h^0)$. The implication is therefore that the error in those results dominated by diffusion may not decrease with the element size.

There are publications that have attempted to address some of these errors. For instance, Ferziger and Peric [2] and Syrakos and Goulas [3] accounted for skewness by using the value and its derivatives at the centre of the line linking two neighbouring cells to interpolate the value at the face centre. Zang *et al.* [4] employed a third-order upwind quadratic scheme to interpolate velocity at the face in curvilinear coordinates. A three-point-based second-order upwind scheme was also used by Hu *et al.* [5]. As pointed by Wu and Hu [1], however, while two of the three points are the centres of neighbouring cells, the third point used in Hu *et al.* [5] is the intersection of the line linking these centres and one of the faces of the cell. The value at the third point is obtained from another interpolation using the centre value of the face and a nodal value which is obtained from further interpolation. The originally intended second-order accuracy may therefore be lost after so many interpolations. For the surface integrals along the face, Lilek and Perić [6] used Simpson's rule based on the centre value of the face and its nodal values. These nodal values had to be obtained by two successive interpolations, although they tried to maintain the same order of accuracy at each interpolation.

In the present work, we shall develop a formulation to deal with all three sources of error mentioned above with a consistent order of accuracy. In addition to velocity and pressure, their spatial derivatives are also introduced at the cell centres. In particular, as the NS equations contain the second-order derivatives of the velocity and first-order derivatives of the pressure, the velocity in the cell is expanded into Taylor series up to the second order whereas the pressure is expanded up to the first order. The derivatives are then obtained through the FVM based on the Gauss theorem. When use of these derivatives is made, the interpolation for the face value is of higher order accuracy, the error due to skewness is eliminated and the numerical integration over the face is calculated by the centre values and its derivatives. All these provide the same order of accuracy as a result.

Several examples are chosen for comparison and validation. The first one is the channel flow where an analytical solution is available, which allows some detailed error analysis to be made. In particular, the present formulation can give the exact solution for this case. This means that the accuracy of the solution is independent to the number of elements used. The error from the numerical simulation is due to the control error in the iteration. The second example is flow past a circular cylinder where a large volume of published data is available. The third example is flow in a collapsible channel. Luo and Pedley [7–10] have published a series of papers on the problem as it has important applications in medical modelling. All these test cases show that the present method is consistent, accurate and flexible.

2. FINITE VOLUME FORMULATION FOR THE NS EQUATIONS

A Cartesian coordinate system $O-xy$ is defined. All the physical parameters are nondimensionalized by the density of the fluid ρ, a typical length of the body D and a typical velocity component U_0. Let ϕ represent either the velocity component u in the x direction or v in the y direction. The nondimensionalized NS equations for ϕ with no gravity effect can be expressed as

$$\frac{\partial \phi}{\partial t} + \nabla(\mathbf{U}\phi) = \frac{1}{Re}\nabla^2\phi - \frac{\partial p}{\partial x_m} \tag{1}$$

where $\mathbf{U}=(u,v)$ is the velocity vector, p is the pressure, $m=1$ corresponds to $\phi=u$ and $m=2$ corresponds to $\phi=v$ and $(x_1,x_2)=(x,y)$. The Reynolds number is $Re=U_0D/v$ and v is the kinematic viscosity of the fluid. To solve the problem, the fluid domain is divided into many small triangular cells. Let h be the typical size of these cells. We can then integrate Equation (1) over a cell V_i centred at point i and bounded by three surfaces A_{fj}, $j=1,2,3$ (see Figure 1). This gives

$$\int_{V_i} \frac{\partial \phi_i}{\partial t}\,\mathrm{d}V + \sum_{j=1}^{3}\int_{A_{fj}}\left((\mathbf{U}\cdot\mathbf{n})\phi - \frac{1}{Re}\frac{\partial \phi}{\partial n}\right)\mathrm{d}A = S^\phi \tag{2}$$

where $\mathbf{n}=(n_{xfj},n_{yfj})$ is the outward normal of the surface. The source term in this equation is defined as

$$S^\phi = -\int_{V_i}\frac{\partial p}{\partial x_m}\,\mathrm{d}V \tag{3}$$

As the variables are defined at cell centres, their values on faces are obtained through interpolation. To achieve that with consistent order of accuracy, we draw a line perpendicular to face fj from the centre point $P(x_{fj},y_{fj})$ of face fj, as shown in Figure 2. If the distance between two cell centre points i and ij is

$$L_{fj} = \sqrt{(x_{ij}-x_i)^2 + (y_{ij}-y_i)^2} \tag{4}$$

points C and D are obtained from

$$x_C = x_{fj} - \frac{L_{fj}}{2}n_{xfj}, \quad y_C = y_{fj} - \frac{L_{fj}}{2}n_{yfj} \tag{5}$$

$$x_D = x_{fj} + \frac{L_{fj}}{2}n_{xfj}, \quad y_D = y_{fj} + \frac{L_{fj}}{2}n_{yfj} \tag{6}$$

Using the Taylor expansion, we have

$$\phi_C = \phi_{fj} - \frac{\partial \phi_{fj}}{\partial L}\left(\frac{L_{fj}}{2}\right) + \frac{1}{2}\frac{\partial^2 \phi_{fj}}{\partial L^2}\left(\frac{L_{fj}}{2}\right)^2 - \frac{1}{6}\frac{\partial^3 \phi_{fj}}{\partial L^3}\left(\frac{L_{fj}}{2}\right)^3 + O(h^4) \tag{7}$$

$$\phi_D = \phi_{fj} + \frac{\partial \phi_{fj}}{\partial L}\left(\frac{L_{fj}}{2}\right) + \frac{1}{2}\frac{\partial^2 \phi_{fj}}{\partial L^2}\left(\frac{L_{fj}}{2}\right)^2 + \frac{1}{6}\frac{\partial^3 \phi_{fj}}{\partial L^3}\left(\frac{L_{fj}}{2}\right)^3 + O(h^4) \tag{8}$$
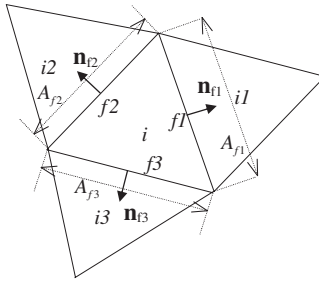
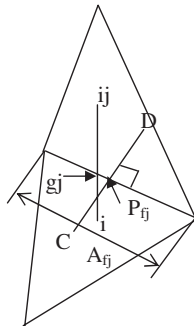Figure 1. A triangular element i with its three neighbours $i1, i2, i3$.

Figure 2. Notation associated with face fj.

in which the derivative is taken in the direction from C to D or the direction of the normal $\mathbf{n}$. Thus,

$$\phi_{fj} = \frac{\phi_C + \phi_D - (\partial^2 \phi_{fj}/\partial L^2)(L_{fj}/2)^2}{2} + O(h^4) \tag{9}$$

The values of ϕ at points C and D can be obtained from the Taylor expansion within the corresponding cells, or

$$\phi_C = \phi_i + \frac{\partial \phi_i}{\partial x}(x_C - x_i) + \frac{\partial \phi_i}{\partial y}(y_C - y_i) + \frac{1}{2}\frac{\partial^2 \phi_i}{\partial x^2}(x_C - x_i)^2 + \frac{1}{2}\frac{\partial^2 \phi_i}{\partial y^2}(y_C - y_i)^2$$

$$+ \frac{1}{2}\left(\frac{\partial^2 \phi_i}{\partial x \partial y} + \frac{\partial^2 \phi_i}{\partial y \partial x}\right)(x_C - x_i)(y_C - y_i) + O(h^3) \tag{10}$$

$$\phi_D = \phi_{ij} + \frac{\partial \phi_{ij}}{\partial x}(x_D - x_{ij}) + \frac{\partial \phi_{ij}}{\partial y}(y_D - y_{ij}) + \frac{1}{2}\frac{\partial^2 \phi_{ij}}{\partial x^2}(x_D - x_{ij})^2 + \frac{1}{2}\frac{\partial^2 \phi_{ij}}{\partial y^2}(y_D - y_{ij})^2$$

$$+ \frac{1}{2}\left(\frac{\partial^2 \phi_{ij}}{\partial x \partial y} + \frac{\partial^2 \phi_{ij}}{\partial y \partial x}\right)(x_D - x_{ij})(y_D - y_{ij}) + O(h^3) \tag{11}$$

Here $\partial^2\phi_{ij}/\partial x\partial y$ and $\partial^2\phi_{ij}/\partial y\partial x$ have been written separately. Although they are identical mathematically, these two terms could be numerically different in the calculation. Taking their average usually provides a better accuracy.

The derivatives in Equations (10) and (11) can be obtained through integrations over the cell. For the first-order ones, we have

$$\frac{1}{V_i}\int_{V_i}\frac{\partial\phi_i}{\partial x}\,\mathrm{d}V=\frac{1}{V_i}\sum_{j=1}^{3}\int_{A_{fj}}\phi n_x\,\mathrm{d}A,\quad \frac{1}{V_i}\int_{V_i}\frac{\partial\phi_i}{\partial y}\,\mathrm{d}V=\frac{1}{V_i}\sum_{j=1}^{3}\int_{A_{fj}}\phi n_y\,\mathrm{d}A \tag{12}$$

which is exact. To calculate the integration over the face fj, we use

$$\phi=\phi_{fj}+\frac{\partial\phi_{fj}}{\partial A}A+\frac{1}{2}\frac{\partial^2\phi_{fj}}{\partial A^2}A^2+\frac{1}{6}\frac{\partial^3\phi_{fj}}{\partial A^3}A^3+O(h^4) \tag{13}$$

where A is measured along the face and $A=-A_{fj}/2$ is the starting point. Since $A_{fj}/V_i=O(1/h)$, we have

$$\frac{\partial\phi_i}{\partial x}+O(h^2)=\frac{1}{V_i}\sum_{j=1}^{3}A_{fj}n_{xfj}\left(\phi_{fj}+\frac{1}{24}\frac{\partial^2\phi_{fj}}{\partial A^2}A_{fj}^2\right)+O(h^3) \tag{14}$$

$$\frac{\partial\phi_i}{\partial y}+O(h^2)=\frac{1}{V_i}\sum_{j=1}^{3}A_{fj}n_{yfj}\left(\phi_{fj}+\frac{1}{24}\frac{\partial^2\phi_{fj}}{\partial A^2}A_{fj}^2\right)+O(h^3) \tag{15}$$

The left-hand sides of Equations (14) and (15) are approximations of those of Equations (12) and (13), obtained from the Taylor expansions of $\partial\phi_i/\partial x$ and $\partial\phi_i/\partial y$. Because the integration of the terms of second derivatives on the left-hand side of Equations (14) and (15) is zero, the error is dominated by the third-order term, which becomes $O(h^2)$ after it is divided by the volume V_i. These two equations are therefore consistent with the principle of the method, which all the terms up to the second order in the Taylor expansion should be retained.

Applying the above procedure to the diffusion term in Equation (2), we obtain

$$-\frac{1}{Re}\frac{1}{V_i}\int_A\frac{\partial\phi}{\partial n}\,\mathrm{d}A=-\frac{1}{Re}\frac{1}{V_i}\sum_{j=1}^{3}\frac{\partial\phi_{fj}}{\partial L_{fj}}A_{fj}+O(h)=-\frac{1}{Re}\frac{1}{V_i}\sum_{j=1}^{3}\frac{\phi_D-\phi_C}{L_{fj}}A_{fj}+O(h) \tag{16}$$

For the convection term, we have

$$I=\frac{1}{V_i}\int_A(\mathbf{U}\cdot\mathbf{n})\phi\,\mathrm{d}A=\frac{1}{V_i}\sum_{j=1}^{3}\left[U_{fj}\phi_{fj}A_{fj}+\frac{1}{24}\frac{\partial^2(U_{fj}\phi_{fj})}{\partial A^2}A_{fj}^3\right]+O(h^3)$$

$$=\frac{1}{2V_i}\sum_j^3 U_{fj}A_{fj}\left[\phi_C+\phi_D-\frac{\partial^2\phi_{fj}}{\partial L^2}\left(\frac{L_{fj}}{2}\right)^2\right]+\frac{1}{24V_i}\sum_{j=1}^{3}\frac{\partial^2(U_{fj}\phi_{fj})}{\partial^2 A^2}A_{fj}^3+O(h^3)$$

$$=\frac{1}{2V_i}\sum_{j=1}^{3}U_{fj}A_{fj}\left[\phi_i+\phi_{ij}+\frac{\partial\phi_i}{\partial x}(x_C-x_i)+\frac{\partial\phi_i}{\partial y}(y_C-y_i)+\frac{1}{2}\frac{\partial^2\phi_i}{\partial x^2}(x_C-x_i)^2\right.$$

$$+\frac{1}{2}\frac{\partial^2\phi_i}{\partial y^2}(y_C-y_i)^2+\frac{1}{2}\left(\frac{\partial^2\phi_i}{\partial x\partial y}+\frac{\partial^2\phi_i}{\partial y\partial x}\right)(x_C-x_i)(y_C-y_i)$$

$$+\frac{\partial\phi_{ij}}{\partial x}(x_D-x_{ij})+\frac{\partial\phi_{ij}}{\partial y}(y_D-y_{ij})+\frac{1}{2}\frac{\partial^2\phi_{ij}}{\partial x^2}(x_D-x_{ij})^2$$

$$+\frac{1}{2}\frac{\partial^2\phi_{ij}}{\partial y^2}(y_D-y_{ij})^2+\frac{1}{2}\left(\frac{\partial^2\phi_{ij}}{\partial x\partial y}+\frac{\partial^2\phi_{ij}}{\partial y\partial x}\right)(x_D-x_{ij})(y_D-y_{ij})$$

$$-\frac{\partial^2\phi_{fj}}{\partial L^2}\left(\frac{L_{fj}}{2}\right)^2\Bigg]+\frac{1}{24V_i}\sum_{j=1}^3\frac{\partial^2(U_{fj}\phi_{fj})}{\partial A^2}A_{fj}^3+O(h^2) \tag{17}$$

ϕ_{fj} in Equation (17) is obtained from the central differencing method in Equation (9). It provides a higher order of spatial accuracy, but it may be prone to instability in the time domain when the Peclet number $Pe=Re|U_{fj}|L>Pe_0$, where Pe_0 is the critical number. In this case, we use the following second-order upwind scheme:

$$I=\frac{1}{V_i}\sum_{j=1}^3U_{fj}A_{fj}\Bigg[\phi_i+\frac{\partial\phi_i}{\partial x}(x_{fj}-x_i)+\frac{\partial\phi_i}{\partial y}(y_{fj}-y_i)$$

$$+\frac{1}{2}\frac{\partial^2\phi_i}{\partial x^2}(x_{fj}-x_i)^2+\frac{1}{2}\frac{\partial^2\phi_i}{\partial y^2}(y_{fj}-y_i)^2+\frac{1}{2}\left(\frac{\partial^2\phi_i}{\partial x\partial y}+\frac{\partial^2\phi_i}{\partial y\partial x}\right)(x_{fj}-x_i)(y_{fj}-y_i)\Bigg]$$

$$+\frac{1}{24V_i}\sum_{j=1}^3\frac{\partial^2(U_{fj}\phi_{fj})}{\partial A^2}A_{fj}^3+O(h^2),\quad U_{fj}>0 \tag{18}$$

$$I=\frac{1}{V_i}\sum_{j=1}^3U_{fj}A_{fj}\Bigg[\phi_{ij}+\frac{\partial\phi_{ij}}{\partial x}(x_{fj}-x_{ij})+\frac{\partial\phi_{ij}}{\partial y}(y_{fj}-y_{ij})$$

$$+\frac{1}{2}\frac{\partial^2\phi_{ij}}{\partial x^2}(x_{fj}-x_{ij})^2+\frac{1}{2}\frac{\partial^2\phi_{ij}}{\partial y^2}(y_{fj}-y_{ij})^2+\frac{1}{2}\left(\frac{\partial^2\phi_{ij}}{\partial x\partial y}+\frac{\partial^2\phi_{ij}}{\partial y\partial x}\right)(x_{fj}-x_{ij})(y_{fj}-y_{ij})\Bigg]$$

$$+\frac{1}{24V_i}\sum_{j=1}^3\frac{\partial^2(U_{fj}\phi_{fj})}{\partial A^2}A_{fj}^3+O(h^2),\quad U_{fj}<0 \tag{19}$$

Substituting above equations into Equation (2), we obtain

$$a_p\phi_i=\sum_{j=1}^3a_{fj}\phi_{fj}+S^\psi+O(h) \tag{20}$$

where

$$a_{fj} = -\frac{1}{2}m_{fj} + \frac{1}{Re}\frac{A_{fj}}{L_{fj}}, \quad a_p = \frac{V_i}{\Delta t} + \sum_{j=1}^{3} b_{fj}, \quad b_{fj} = \frac{1}{2}m_{fj} + \frac{1}{Re}\frac{A_{fj}}{L_{fj}}, \quad m_{fj} = U_{fj}A_{fj} \quad (21)$$

$$S^{\psi} = S^{\phi} + S_2^{\psi} + S_3^{\psi} + \frac{V_i}{\Delta t}\phi_{i0} \quad (22)$$

$$S_2^{\psi} = -\frac{1}{2}\sum_{j=1}^{3} m_{fj}\left[\frac{\partial\phi_i}{\partial x}(x_C - x_i) + \frac{\partial\phi_i}{\partial y}(y_c - y_i) + \frac{1}{2}\frac{\partial^2\phi_i}{\partial x^2}(x_C - x_i)^2 + \frac{1}{2}\frac{\partial^2\phi_i}{\partial y^2}(y_C - y_i)^2\right.$$

$$+ \frac{1}{2}\left(\frac{\partial^2\phi_i}{\partial x\partial y} + \frac{\partial^2\phi_i}{\partial y\partial x}\right)(x_C - x_i)(y_C - y_i) + \frac{\partial\phi_{ij}}{\partial x}(x_D - x_{ij}) + \frac{\partial\phi_{ij}}{\partial y}(y_D - y_i)$$

$$+ \frac{1}{2}\frac{\partial^2\phi_{ij}}{\partial x^2}(x_D - x_{ij})^2 + \frac{1}{2}\frac{\partial^2\phi_{ij}}{\partial y^2}(y_D - y_{ij})^2 + \frac{1}{2}\left(\frac{\partial^2\phi_{ij}}{\partial x\partial y} + \frac{\partial^2\phi_{ij}}{\partial y\partial x}\right)(x_D - x_{ij})(y_D - y_{ij})$$

$$\left. - \frac{\partial^2\phi_{fj}}{\partial L^2}\left(\frac{L_{fj}}{2}\right)^2\right] - \frac{1}{24V_i}\sum_{j=1}^{3}\frac{\partial^2(U_{fj}\phi_{fj})}{\partial A^2}A_{fj}^3 \quad (23)$$

$$S_3^{\psi} = \frac{1}{Re}\sum_{j=1}^{3}\frac{A_{fj}}{L_{fj}}\left\{\left[\frac{\partial\phi_{ij}}{\partial x}(x_D - x_{ij}) + \frac{\partial\phi_{ij}}{\partial y}(y_D - y_{ij}) + \frac{1}{2}\frac{\partial^2\phi_{ij}}{\partial x^2}(x_D - x_{ij})^2\right.\right.$$

$$\left. + \frac{1}{2}\frac{\partial^2\phi_{ij}}{\partial y^2}(y_D - y_{ij})^2 + \frac{1}{2}\left(\frac{\partial^2\phi_{ij}}{\partial x\partial y} + \frac{\partial^2\phi_{ij}}{\partial y\partial x}\right)(x_D - x_{ij})(y_D - y_{ij})\right]$$

$$- \left[\frac{\partial\phi_i}{\partial x}(x_C - x_i) + \frac{\partial\phi_i}{\partial y}(y_C - y_i) + \frac{1}{2}\frac{\partial^2\phi_i}{\partial x^2}(x_C - x_i)^2 + \frac{1}{2}\frac{\partial^2\phi_i}{\partial y^2}(y_C - y_i)^2\right.$$

$$\left.\left. + \frac{1}{2}\left(\frac{\partial^2\phi_i}{\partial x\partial y} + \frac{\partial^2\phi_i}{\partial y\partial x}\right)(x_C - x_i)(y_C - y_i)\right]\right\} \quad (24)$$

when $Pe < Pe_0$. When $Pe \geqslant Pe_0$ on face fj, we have

$$b_{fj} = \begin{cases} m_{fj} + \frac{1}{Re}\frac{A_{fj}}{L_{fj}}, & U_{fj} > 0, \\ \frac{1}{Re}\frac{A_{fj}}{L_{fj}}, & U_{fj} < 0, \end{cases} \quad a_{fj} = \begin{cases} \frac{1}{Re}\frac{A_{fj}}{L_{fj}}, & U_{fj} > 0 \\ -m_{fj} + \frac{1}{Re}\frac{A_{fj}}{L_{fj}}, & U_{fj} < 0 \end{cases} \quad (25)$$

and the fj term in S_2^{ψ} becomes

$$-m_{fj}\left[\frac{\partial\phi_{fj}}{\partial x}(x_{fj}-x_i)+\frac{\partial\phi_{fj}}{\partial y}(y_{fj}-y_i)+\frac{1}{2}\frac{\partial^2\phi_i}{\partial x^2}(x_{fj}-x_i)^2+\frac{1}{2}\frac{\partial^2\phi_i}{\partial y^2}(y_{fj}-y_i)^2\right.$$

$$\left.+\frac{1}{2}\left(\frac{\partial^2\phi_i}{\partial x\partial y}+\frac{\partial^2\phi_i}{\partial y\partial x}\right)(x_{fj}-x_i)(y_{fj}-y_i)\right]-\frac{1}{24V_i}\frac{\partial^2(U_{fj}\phi_{fj})}{\partial A^2}A_{fj}^3,\quad U_{fj}>0 \qquad (26)$$

$$-m_{fj}\left[\frac{\partial\phi_{ij}}{\partial x}(x_{fj}-x_{ij})+\frac{\partial\phi_{ij}}{\partial y}(y_{fj}-y_{ij})+\frac{1}{2}\frac{\partial^2\phi_{ij}}{\partial x^2}(x_{fj}-x_{ij})^2+\frac{1}{2}\frac{\partial^2\phi_{ij}}{\partial y^2}(y_{fj}-y_{ij})^2\right.$$

$$\left.+\frac{1}{2}\left(\frac{\partial^2\phi_{ij}}{\partial x\partial y}+\frac{\partial^2\phi_{ij}}{\partial y\partial x}\right)(x_{fj}-x_{ij})(y_{fj}-y_{ij})\right]-\frac{1}{24V_i}\frac{\partial^2(U_{fj}\phi_{fj})}{\partial A^2}A_{fj}^3,\quad U_{fj}<0 \qquad (27)$$

Equation (20) provides a procedure for iteration to obtain the solution for ϕ_i at current time t. The solution at previous time ϕ_{i0} is included in the source term in Equation (22). At $t+\Delta t$, ϕ_i is used to replace ϕ_{i0} and this forms the time stepping method. When the semi-implicit scheme is used, the coefficients a_p and a_{fj} at t can be obtained from the solution at the previous time step or from ϕ_{i0}. For the fully implicit scheme, they can be obtained from the latest results of ϕ_i during the iteration at the current time step. The former is used in the present paper. The first-order derivatives required in the source terms S_2^{ψ} and S_3^{ψ} in Equation (20) can be obtained from Equations (14) and (15). For the second-order derivatives, we define ψ as $\partial\phi_i/\partial x$ and χ as $\partial\phi_i/\partial y$. We then have

$$\frac{\partial\psi_i}{\partial x}=\frac{1}{V_i}\sum_{j=1}^{3}A_{fj}n_{xfj}\left\{\psi_{gj}+\frac{\partial\psi_{gj}}{\partial A}[-(x_{fj}-x_{gj})n_{yfj}+(y_{fj}-y_{gj})n_{xfj}]+O(h)\right\} \qquad (28)$$

$$\frac{\partial\psi_i}{\partial y}=\frac{1}{V_i}\sum_{j=1}^{3}A_{fj}n_{yfj}\left\{\psi_{gj}+\frac{\partial\psi_{gj}}{\partial A}[-(x_{fj}-x_{gj})n_{yfj}+(y_{fj}-y_{gj})n_{xfj}]+O(h)\right\} \qquad (29)$$

$$\frac{\partial\chi_i}{\partial x}=\frac{1}{V_i}\sum_{j=1}^{3}A_{fj}n_{xfj}\left\{\chi_{gj}+\frac{\partial\chi_{gj}}{\partial A}[-(x_{fj}-x_{gj})n_{yfj}+(y_{fj}-y_{gj})n_{xfj}]+O(h)\right\} \qquad (30)$$

$$\frac{\partial\chi_i}{\partial y}=\frac{1}{V_i}\sum_{j=1}^{3}A_{fj}n_{yfj}\left\{\chi_{gj}+\frac{\partial\chi_{gj}}{\partial A}[-(x_{fj}-x_{gj})n_{yfj}+(y_{fj}-y_{gj})n_{xfj}]+O(h)\right\} \qquad (31)$$

where (x_{gj}, y_{gj}) is the intersection point between the line linking i and ij and face fj. Thus,

$$\psi_{gj}=\lambda_j\psi_i+(1-\lambda_j)\psi_{ij}+O(h^2),\quad \chi_{gj}=\lambda_j\chi_i+(1-\lambda_j)\chi_{ij}+O(h^2) \qquad (32)$$

where

$$\lambda_j=\frac{\sqrt{(x_{ij}-x_{gj})^2+(y_{ij}-y_{gj})^2}}{\sqrt{(x_{ij}-x_i)^2+(y_{ij}-y_i)^2}} \qquad (33)$$

From these equations, the second-order derivatives in the normal direction and along the face can be found using

$$\frac{\partial^2 \phi_{fj}}{\partial L^2} = \frac{\partial^2 \phi_{fj}}{\partial x^2} n_{xfj}^2 + \left(\frac{\partial^2 \phi_{fj}}{\partial x \partial y} + \frac{\partial^2 \phi_{fj}}{\partial y \partial x} \right) n_{xfj} n_{yfj} + \frac{\partial^2 \phi_{fj}}{\partial y^2} n_{yfj}^2 \tag{34}$$

$$\frac{\partial^2 \phi_{fj}}{\partial A^2} = \frac{\partial^2 \phi_{fj}}{\partial x^2} n_{yfj}^2 - \left(\frac{\partial^2 \phi_{fj}}{\partial x \partial y} + \frac{\partial^2 \phi_{fj}}{\partial y \partial x} \right) n_{xfj} n_{yfj} + \frac{\partial^2 \phi_{fj}}{\partial y^2} n_{xfj}^2 \tag{35}$$

where

$$\frac{\partial^2 \phi_{fj}}{\partial x^2} = \frac{\partial^2 \phi_{gj}}{\partial x^2} + O(h) = \lambda_j \frac{\partial \psi_i}{\partial x} + (1 - \lambda_j) \frac{\partial \psi_{ij}}{\partial x} + O(h) \tag{36}$$

$$\frac{\partial^2 \phi_{fj}}{\partial y \partial x} = \frac{\partial^2 \phi_{gj}}{\partial y \partial x} + O(h) = \lambda_j \frac{\partial \psi_i}{\partial y} + (1 - \lambda_j) \frac{\partial \psi_{ij}}{\partial y} + O(h) \tag{37}$$

$$\frac{\partial^2 \phi_{fj}}{\partial x \partial y} = \frac{\partial^2 \phi_{gj}}{\partial x \partial y} + O(h) = \lambda_j \frac{\partial \chi_i}{\partial x} + (1 - \lambda_j) \frac{\partial \chi_{ij}}{\partial x} + O(h) \tag{38}$$

$$\frac{\partial^2 \phi_{fj}}{\partial y^2} = \frac{\partial^2 \phi_{gj}}{\partial y^2} + O(h) = \lambda_j \frac{\partial \chi_i}{\partial y} + (1 - \lambda_j) \frac{\partial \chi_{ij}}{\partial y} + O(h) \tag{39}$$

Finally for the source term due to pressure, we have

$$\frac{\partial p_i}{\partial x_m} = \frac{1}{V_i} \int_A p n_m \, \mathrm{d}A + O(h) = \frac{1}{V_i} \sum_{j=1}^{3} n_{mfj} A_{fj} p_{fj} + O(h)$$

$$= \frac{1}{2V_i} \sum_{j=1}^{3} n_{mfj} A_{fj} \left[p_i + p_{ij} + \frac{\partial p_i}{\partial x}(x_C - x_i) + \frac{\partial p_i}{\partial y}(y_C - y_i) \right.$$

$$\left. + \frac{\partial p_{ij}}{\partial x}(x_D - x_{ij}) + \frac{\partial p_{ij}}{\partial y}(y_D - y_{ij}) \right] + O(h) \tag{40}$$

When fj is on the boundary, the above procedure has to be modified. For the Dirichlet boundary condition $\phi = \Phi$, the integration of the convection term over this face can be found from

$$I_{fj} = \frac{1}{V_i} \int_{A_{fj}} (\mathbf{U}\phi) \mathbf{n} \, \mathrm{d}A = \frac{1}{V_i} \left[m_{fj} \Phi_{fj} + \frac{1}{24} \frac{\partial^2 (U_{fj} \Phi_{fj})}{\partial A^2} A_{fj}^3 \right] + O(h^3) \tag{41}$$

or can be obtained analytically. For the diffusion term, we link points i and fj to form line L, which has an angle β with the x-axis. If the centre of L is Q, we have (see Figure 3)

$$\frac{\partial \phi_Q}{\partial L} = \frac{\Phi_{fj} - \phi_i}{L} + O(h^2) \tag{42}$$

$$\frac{\partial \phi_{fj}}{\partial L} = 2\frac{\partial \phi_Q}{\partial L} - \frac{\partial \phi_i}{\partial L} + O(h^2) \tag{43}$$

Since

$$\frac{\partial \phi_{fj}}{\partial L} = \frac{\partial \phi_{fj}}{\partial x}\cos\beta + \frac{\partial \phi_{fj}}{\partial y}\sin\beta \tag{44}$$

$$\frac{\partial \Phi_{fj}}{\partial A} = -\frac{\partial \phi_{fj}}{\partial x}n_{yfj} + \frac{\partial \phi_{fj}}{\partial y}n_{xfj} \tag{45}$$

Thus,

$$\frac{\partial \phi_{fj}}{\partial x} = \frac{(\partial \phi_{fj}/\partial L)n_{xfj} - (\partial \Phi_{fj}/\partial A)\sin\beta}{n_{xfj}\cos\beta + n_{yfj}\sin\beta} \tag{46}$$

$$\frac{\partial \phi_{fj}}{\partial y} = \frac{(\partial \Phi_{fj}/\partial A)\cos\beta + (\partial \phi_{fj}/\partial L)n_{yfj}}{n_{xfj}\cos\beta + n_{yfj}\sin\beta} \tag{47}$$

For the derivatives required in Equations (28) and (31), we have

$$\frac{\partial}{\partial A}\left(\frac{\partial \phi_{fj}}{\partial x}\right) = \frac{(\partial^2 \phi_{fj}/\partial A\partial L)n_{xfj} - (\partial^2 \Phi_{fj}/\partial A^2)\sin\beta}{n_{xfj}\cos\beta + n_{yfj}\sin\beta} \tag{48}$$

$$\frac{\partial}{\partial A}\left(\frac{\partial \phi_{fj}}{\partial y}\right) = \frac{(\partial^2 \Phi_{fj}/\partial A^2)\cos\beta + (\partial^2 \phi_{fj}/\partial A\partial L)n_{yfj}}{n_{xfj}\cos\beta + n_{yfj}\sin\beta} \tag{49}$$

where

$$\frac{\partial^2 \phi_{fj}}{\partial A\partial L} = \frac{2}{L}\left(\frac{\partial \Phi_{fj}}{\partial A} - \frac{\partial \phi_i}{\partial A}\right) - \frac{\partial^2 \phi_i}{\partial A\partial L} + O(h) \tag{50}$$

In reality, we can choose $(x_{fj}, y_{fj}) = (x_{gj}, y_{gj})$ on the boundary. As a result, the derivatives in Equations (48) and (49) will have no effect on Equations (28)–(31).

For the diffusion term on face fj, we can express

$$-\frac{1}{V_i}\frac{A_{fj}}{Re}\frac{\partial \phi_{fj}}{\partial n} = -\frac{1}{V_i}\frac{A_{fj}}{Re}\frac{\partial \phi_{fj}/\partial L + (\partial \Phi_{fj}/\partial A)(n_{yfj}\cos\beta - n_{xfj}\sin\beta)}{n_{xfj}\cos\beta + n_{yfj}\sin\beta} \tag{51}$$
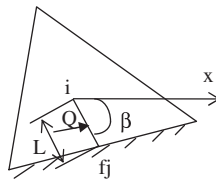

Figure 3. Notation associated with face fj on Dirichlet boundary.

As a result of all these, we have

$$a_{fj} = 0, \quad b_{fj} = \frac{A_{fj}}{Re} \frac{2}{n_{xfj}(x_{fj} - x_i) + n_{yfj}(y_{fj} - y_i)} \tag{52}$$

Also the source terms due to face fj in S_2^ψ and S_3^ψ should be deleted. Instead a new source term

$$-V_i I_{fj} + \frac{A_{fj}}{Re} \left[\frac{2\phi_{fj}}{n_{xfj}(x_{fj} - x_i) + n_{yfj}(y_{fj} - y_i)} \right.$$

$$\left. + \frac{-\partial \phi_i / \partial L + (\partial \Phi_{fj} / \partial A)(n_{yfj} \cos \beta - n_{xfj} \sin \beta)}{n_{xfj} \cos \beta + n_{yfj} \sin \beta} \right] \tag{53}$$

should be added.

When fj is on the boundary with Neumann condition $\partial \phi / \partial n = \Psi$, draw a line M passing the cell centre i and parallel to fj. Let Q be a point on M and P a point on face fj, and PQ be perpendicular to fj. If $PQ = L = L_{fj}/2$, we have

$$\frac{\phi_P - \phi_Q}{L} = \frac{1}{2} \left(\Psi_P + \frac{\partial \phi_Q}{\partial L} \right) + O(h^2)$$

$$= \frac{1}{2} \left(\Psi_P + \frac{\partial \phi_Q}{\partial x} n_{xfj} + \frac{\partial \phi_Q}{\partial y} n_{yfj} \right) + O(h^2) \tag{54}$$

Using Equation (10), we obtain

$$\frac{\phi_P - \phi_Q}{L} = \frac{1}{2} \left\{ \Psi_P + \left[\frac{\partial \phi_i}{\partial x} + \frac{\partial^2 \phi_i}{\partial x^2}(x_Q - x_i) + \frac{1}{2}\left(\frac{\partial^2 \phi_i}{\partial x \partial y} + \frac{\partial^2 \phi_i}{\partial y \partial x} \right)(y_Q - y_i) \right] n_{xfj} \right.$$

$$\left. + \left[\frac{\partial \phi_i}{\partial y} + \frac{\partial^2 \phi_i}{\partial y^2}(y_Q - y_i) + \frac{1}{2}\left(\frac{\partial^2 \phi_i}{\partial x \partial y} + \frac{\partial^2 \phi_i}{\partial y \partial x} \right)(y_Q - y_i) \right] n_{yfj} \right\} + O(h^2) \tag{55}$$

Thus at the centre of the face, we have

$$\phi_{fj} = \phi_C + \frac{L}{2} \left\{ \Psi_{fj} + \left[\frac{\partial \phi_i}{\partial x} + \frac{\partial^2 \phi_i}{\partial x^2}(x_C - x_i) + \frac{1}{2}\left(\frac{\partial^2 \phi_i}{\partial x \partial y} + \frac{\partial^2 \phi_i}{\partial y \partial x} \right)(y_C - y_i) \right] n_{xfj} \right.$$

$$\left. + \left[\frac{\partial \phi_i}{\partial y} + \frac{\partial^2 \phi_i}{\partial y^2}(y_C - y_i) + \frac{1}{2}\left(\frac{\partial^2 \phi_i}{\partial x \partial y} + \frac{\partial^2 \phi_i}{\partial y \partial x} \right)(x_C - x_i) \right] n_{yfj} \right\} + O(h^3) \tag{56}$$

where

$$x_C = x_{fj} - n_{xfj}L, \quad y_C = y_{fj} - n_{yfj}L \tag{57}$$

From Equation (55), we also obtain

$$
\begin{aligned}
\frac{\partial \phi_{fj}}{\partial A} &= \frac{\partial \phi_i}{\partial A} - \frac{\partial^2 \phi_i}{\partial x^2}(x_C - x_i)n_{yfj} + \frac{\partial^2 \phi_i}{\partial y^2}(y_C - y_i)n_{xfj} \\
&\quad + \frac{1}{2}\left(\frac{\partial^2 \phi_i}{\partial x \partial y} + \frac{\partial^2 \phi_i}{\partial y \partial x}\right)[-(y_C - y_i)n_{yfj} + (x_C - x_i)n_{xfj}] \\
&\quad + \frac{L}{2}\left[\frac{\partial \Psi_{fj}}{\partial A} + \left(-\frac{\partial^2 \phi_i}{\partial x^2} + \frac{\partial^2 \phi_i}{\partial y^2}\right)n_{xfj}n_{yfj} + \frac{1}{2}\left(\frac{\partial^2 \phi_i}{\partial x \partial y} + \frac{\partial^2 \phi_i}{\partial y \partial x}\right)(n_{xfj}^2 - n_{yfj}^2)\right] + O(h^2) \\
&= \frac{\partial \phi_i}{\partial A} - \frac{\partial^2 \phi_i}{\partial x^2}(x_{fj} - x_i)n_{yfj} + \frac{\partial^2 \phi_i}{\partial y^2}(y_{fj} - y_i)n_{xfj} \\
&\quad + \frac{1}{2}\left(\frac{\partial^2 \phi_i}{\partial x \partial y} + \frac{\partial^2 \phi_i}{\partial y \partial x}\right)[-(y_{fj} - y_i)n_{yfj} + (x_{fj} - x_i)n_{xfj}] \\
&\quad + \frac{L}{2}\left[\frac{\partial \Psi_{fj}}{\partial A} + \left(\frac{\partial^2 \phi_i}{\partial x^2} - \frac{\partial^2 \phi_i}{\partial y^2}\right)n_{xfj}n_{yfj}\right] + O(h^2)
\end{aligned}
\tag{58}
$$

$$
\frac{\partial^2 \phi_{fj}}{\partial A^2} = \frac{\partial^2 \phi_i}{\partial x^2}n_{yfj}^2 + \frac{\partial^2 \phi_i}{\partial y^2}n_{xfj}^2 - \left(\frac{\partial^2 \phi_i}{\partial x \partial y} + \frac{\partial^2 \phi_i}{\partial y \partial x}\right)n_{xfj}n_{yfj} + \frac{L}{2}\frac{\partial^2 \Psi_{fj}}{\partial A^2} + O(h)
\tag{59}
$$

Using Equation (59), the integration of the convection term over fj becomes

$$
\begin{aligned}
I_{fj} &= \frac{1}{V_i}\int_{A_{fj}}(\mathbf{U}\phi)\mathbf{n}\,dA = \frac{1}{V_i}\left[m_{fj}\phi_{fj} + \frac{1}{24}\frac{\partial^2(U_{fj}\phi_{fj})}{\partial A^2}A_{fj}^3\right] + O(h^2) \\
&= \frac{1}{V_i}(m_{fj}\phi_i + S_I) + O(h^2)
\end{aligned}
\tag{60}
$$

where

$$
\begin{aligned}
S_I &= m_{fj}\left[\frac{\partial \phi_i}{\partial x}(x_C - x_i) + \frac{\partial \phi_i}{\partial y}(y_C - y_i) + \frac{1}{2}\frac{\partial^2 \phi_i}{\partial x^2}(x_C - x_i)^2 + \frac{1}{2}\frac{\partial^2 \phi_i}{\partial y^2}(y_C - y_i)^2\right. \\
&\quad \left. + \frac{1}{2}\left(\frac{\partial^2 \phi_i}{\partial x \partial y} + \frac{\partial^2 \phi_i}{\partial y \partial x}\right)(x_C - x_i)(y_C - y_i)\right] \\
&\quad + \frac{m_{fj}L}{2}\left\{\Psi_{fj} + \left[\frac{\partial \phi_i}{\partial x} + \frac{\partial^2 \phi_i}{\partial x^2}(x_C - x_i) + \frac{1}{2}\left(\frac{\partial^2 \phi_i}{\partial x \partial y} + \frac{\partial^2 \phi_i}{\partial y \partial x}\right)(y_C - y_i)\right]n_{xfj}\right.
\end{aligned}
$$

$$+\left[\frac{\partial\phi_i}{\partial y}+\frac{\partial^2\phi_i}{\partial y^2}(y_C-y_i)+\frac{1}{2}\left(\frac{\partial^2\phi_i}{\partial x\partial y}+\frac{\partial^2\phi_i}{\partial y\partial x}\right)(x_C-x_i)\right]n_{yfj}\bigg\}$$

$$+\frac{1}{24}\frac{\partial^2(U_{fj}\phi_{fj})}{\partial A^2}A_{fj}^3 \tag{61}$$

Here the order of accuracy of Equation (60) is $O(h^2)$ because of Equation (59).

The integration of the diffusion term over fj can be calculated analytically, or

$$-\frac{1}{Re}\frac{1}{V_i}\int_{A_{fj}}\frac{\partial\phi}{\partial n}\,dA=-\frac{1}{Re}\frac{1}{V_i}\int_{A_{fj}}\Psi\,dA \tag{62}$$

As a result of all these we have

$$a_{fj}=0,\quad b_{fj}=m_{fj} \tag{63}$$

Also the source terms due to face fj in S_2^ψ and S_3^ψ should be deleted. Instead a new source term

$$-S_I+\frac{1}{Re}\int_{A_{fj}}\Psi\,dA \tag{64}$$

should be added.

It would be appropriate at this stage to compare the scheme with that developed by Lehnhauser and Schafer [11]. They also used the Taylor expansion to improve the accuracy in a different manor. However, they did not include the second-order derivative in the analysis. For instance, the flux across a face is calculated simply by multiplying the velocity at the face centre with the face area, whereas in this paper Equation (14) is used, which includes the second-order derivative. Thus, once again the present paper includes all the second derivatives. This leads the method to be more accurate. In fact it becomes exact for the steady channel flow, which is to be discussed in detail later.

3. PRESSURE CORRECTION THROUGH THE SIMPLE TECHNIQUE

The solution of Equation (20) does not automatically satisfy the continuity equation. This is usually achieved through adjusting the pressure distribution and the so-called SIMPLE algorithm [12] is one of the most commonly used. Here the method is adopted after some modifications, which is summarized below. It starts by assuming an initial pressure distribution p^+ with a velocity field ϕ^+. Equation (20) can then be expressed as

$$a_p\phi_i^*=\sum_{j=1}^{3}a_{fj}\phi_{ij}^+-\left(\frac{\partial p^+}{\partial x_m}\right)_i V_i+S \tag{65}$$

where S contains all the source terms apart that due to pressure. The new velocity field ϕ^* may not satisfy the required continuity equation. Thus a pressure correction p' is introduced, or

$$p=p^++p' \tag{66}$$

Putting this into Equation (65), we have

$$a_p \phi_i = \sum_{j=1}^{3} a_{fj} \phi_{ij}^{+} - \left[\frac{\partial (p^{+} + p')}{\partial x_m} \right]_i V_i + S \tag{67}$$

Subtraction of Equation (65) from (67) then gives

$$u_i = u_i^{*} - \alpha_i \frac{\partial p_i'}{\partial x} \tag{68}$$

$$v_i = v_i^{*} - \alpha_i \frac{\partial p_i'}{\partial y} \tag{69}$$

where $\alpha_i = V_i / a_p$. We require the new velocity field u_i and v_i to satisfy the continuity equation:

$$\frac{\partial u_i}{\partial x} + \frac{\partial v_i}{\partial y} = 0 \tag{70}$$

which can be expressed as

$$\frac{\partial u_i^{*}}{\partial x} + \frac{\partial v_i^{*}}{\partial y} - \frac{\partial}{\partial x} \left(\alpha_i \frac{\partial p_i'}{\partial x} \right) - \frac{\partial}{\partial y} \left(\alpha_i \frac{\partial p_i'}{\partial y} \right) = 0 \tag{71}$$

Integrating over the cell, we obtain

$$V_i \left(\frac{\partial u_i^{*}}{\partial x} + \frac{\partial v_i^{*}}{\partial y} \right) - \sum_{j=1}^{3} \alpha_{fj} \frac{\partial p_{fj}'}{\partial n} A_{fj} = 0 \tag{72}$$

in which the derivatives of the velocity are obtained from Equations (14) and (15). For the normal derivative of p' on the surface, we can use Equations (5) and (6) to express

$$\begin{aligned}
\alpha_{fj} \frac{\partial p_{fj}'}{\partial n} &= \frac{1}{2L_{fj}} (\alpha_C + \alpha_D)(p_D' - p_C') \\
&= \frac{1}{2L_{fj}} \left[\alpha_i + \frac{\partial \alpha_i}{\partial x}(x_C - x_i) + \frac{\partial \alpha_i}{\partial y}(y_C - y_i) + \alpha_{ij} + \frac{\partial \alpha_{ij}}{\partial x}(x_D - x_{ij}) + \frac{\partial \alpha_{ij}}{\partial y}(y_D - y_{ij}) \right] \\
&\quad \times \left[p_{ij}' + \frac{\partial p_{ij}'}{\partial x}(x_D - x_{ij}) + \frac{\partial p_{ij}'}{\partial y}(y_D - y_{ij}) - p_i' \right. \\
&\quad \left. - \frac{\partial p_i'}{\partial x}(x_C - x_i) - \frac{\partial p_j'}{\partial y}(y_C - y_i) \right]
\end{aligned} \tag{73}$$

This gives

$$a_i p_i' = a_{pf1} p_{i1}' + a_{pf2} p_{i2}' + a_{pf3} p_{i3}' + S_p \tag{74}$$

where

$$a_{pfj} = \frac{A_{fj}}{2L_{fj}} \left[\alpha_i + \frac{\partial \alpha_i}{\partial x}(x_C - x_i) + \frac{\partial \alpha_i}{\partial y}(y_C - y_i) + \alpha_{ij} + \frac{\partial \alpha_{ij}}{\partial x}(x_D - x_{ij}) + \frac{\partial \alpha_{ij}}{\partial y}(y_D - y_{ij}) \right] \quad (75)$$

$$a_i = a_{pf1} + a_{pf2} + a_{pf3} \quad (76)$$

$$S_p = -V_i \left(\frac{\partial u_i^*}{\partial x} + \frac{\partial v_i^*}{\partial y} \right)$$

$$+ \sum_{j=1}^{3} a_{pfj} \left[\frac{\partial p'_{ij}}{\partial x}(x_D - x_{ij}) + \frac{\partial p'_{ij}}{\partial y}(y_D - y_{ij}) - \frac{\partial p'_i}{\partial x}(x_C - x_i) - \frac{\partial p'_i}{\partial y}(y_C - y_i) \right] \quad (77)$$

The derivatives of α and p' with respect to x and y can be obtained in a manner similar to that in Equation (40). Equation (74) is solved based on the iteration similar to Equation (20). In fact, iteration is usually carried out only a few times. The obtained p'_i is then used for pressure and velocity corrections in Equations (65), (68) and (69). This normally leads a faster convergence of the solutions for the momentum and continuity equations.

4. RESULTS

The present FVM formulation may appear to be a bit lengthy. However, careful inspection can easily show that the method does not bring any new real complexity. The format itself of Equation (20) is, for example, virtually identical to that used in the other FVM (e.g. [1]). The difference is in the details of the coefficients and the source term, but they can be easily calculated from the geometrical configuration of the mesh. The CPU requirement for the extra computation of these coefficients itself is insignificant. However, as the first and second derivatives of the velocity have now entered the iteration through Equations (14) and (15), and through Equations (28)–(39), they may converge much more slowly than the velocity itself if the same degree of accuracy is needed. Thus, the extra CPU required is not mainly for the extra terms in the equations, but for the more accurate results of the shear force and diffusion.

The solution starts from mesh generation that is based on a Delaunay triangulation and the procedure is in Giraldo [13]. Initial values of the velocities, u, v, and the pressure, p, are set in all the cell centres. Equation (20) is used to update the velocity and Equation (74) is used for pressure correction. The process is repeated until the difference between the current result and that at the previous iteration in the momentum equation falls below 1.0×10^{-6} and the error in the continuity equation falls below 1.0×10^{-4}, or $\partial u_i/\partial x + \partial v_i/\partial y < 1.0 \times 10^{-4}$ at every cell.

4.1. Channel flow

We consider the flow in a rectangular channel for validation. The width of channel D is the length scale used for nondimension and the x-axis is taken along the lower wall of the channel. The analytical solution for the one-dimensional flow driven by a constant pressure gradient dp/dx can then be expressed as

$$u = -\frac{Re}{2}\frac{dp}{dx}(y - y^2), \quad v = 0 \quad (78)$$

Careful examination of the present formulation shows that almost no approximation is made in the analysis for this problem. Take Equations (14) and (15), for example. If one applies the Taylor expansion on the left-hand sides of these two equations, there will be a second-order derivative term. However, this term will disappear after integration over the cell. On the right-hand sides of these two equations, all the terms from the Taylor expansion have been included. Thus, these two equations are exact in this case. The only approximation in this problem is made in Equation (17) [and subsequently in Equation (41)]. If the Taylor expansion was applied to $\mathbf{U}\cdot\mathbf{n}$ and ϕ separately rather to the combined $(\mathbf{U}\cdot\mathbf{n})\phi$, an extra term $(1/320)(\partial^2 U_{fj}/\partial A^2)(\partial^2 \phi/\partial A^2)A_{fj}^5$ would have appeared. However, this term would not make too much difference in practice, as a mesh with elements of typical size $h=O(10^{-1})$ will lead to a coefficient of order $O(10^{-7})$ in this term.

We consider a case with $Re=96$ and $\mathrm{d}p/\mathrm{d}x=-0.125$. The velocity is prescribed at the inlet on the left-hand side of the channel, whereas the Neumann condition is used at the outlet. No-slip condition is used on the side walls. The initial values of the velocity and pressure are taken as zero at all cell centres. Three different meshes with $h=0.1, 0.05, 0.025$ are used as shown in Figures 4–6. Table I gives the details of the meshes and the results at $t=10$. The error is defined as the largest difference between the analytical solution and the numerical result. As expected, the error corresponding to $h=0.1$ is already sufficiently small. In fact it can be further reduced if the control errors in the momentum equations and continuity equation discussed at the beginning of Section 4 are reduced. The result therefore shows that the present formulation is quite accurate. Figure 7 shows the pressure contour from the simulation. As in the analytical solution, the pressure is constant at a given value of x. Streamlines are given in Figure 8, which are parallel to the side walls as in the analytical solution.

4.2. Flow past a fixed cylinder

Flow past a cylinder is a standard test case and is widely used for validation of computational fluid dynamics methods. The computational configuration used for the present simulation is shown in Figure 9 with $\mathrm{Le}=20D$, $\mathrm{Lr}=20D$ and $\mathrm{Ls}=20D$, where D is the diameter of the cylinder and is the length scale used for nondimensionalization. We consider a case at $Re=40$. Grid convergence
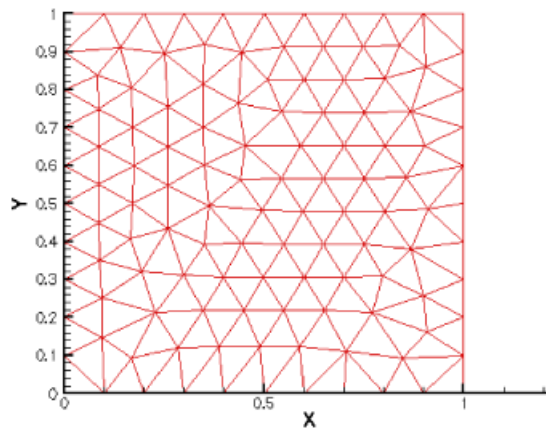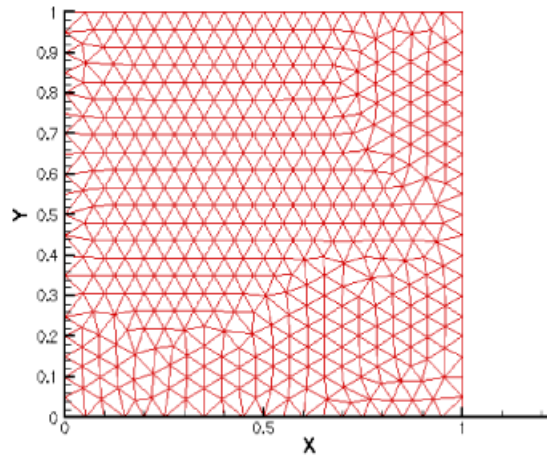

Figure 4. Entire grid for channel flow (case 1).
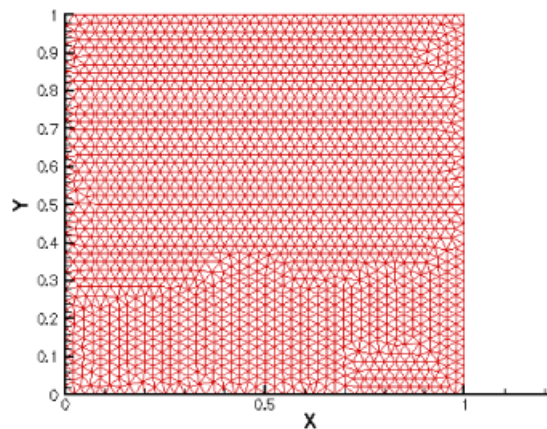
Figure 5. Entire grid for channel flow (case 2).

Figure 6. Entire grid for channel flow (case 3).

Table I. Errors of u in the 'exact' numerical solution for channel flow at $Re = 96.0$.

Case	Number of cells	Number of nodes	Error
1, $h = 0.100$	202	122	7.985E−007
2, $h = 0.050$	870	476	2.369E−007
3, $h = 0.025$	3580	1871	6.608E−008

was carried out by three meshes as listed in Table II, where h is the size of a typical element on the cylinder surface. The mesh structure near the cylinder corresponding to mesh 2 is shown in Figure 10. In the unsteady flow, the time step is not only crucial for accuracy but also important for stability. For a structured mesh, some relationships between the time step and element size
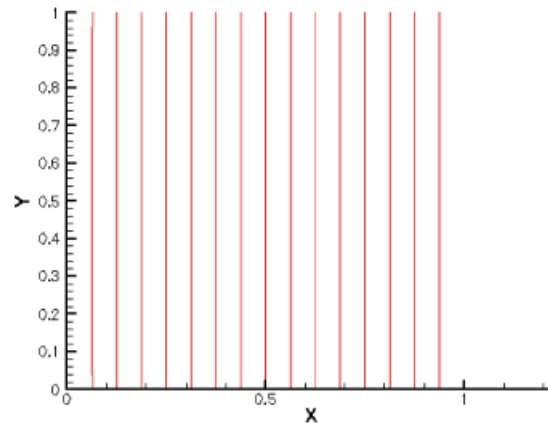
Figure 7. Pressure contours for channel flow at $Re = 96.0$.
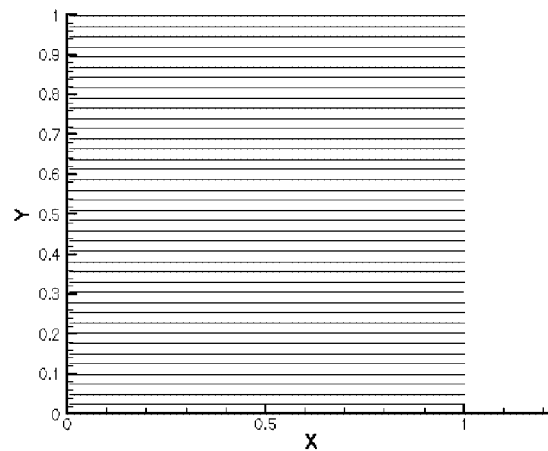
Figure 8. Streamlines for channel flow at $Re = 96.0$.

may be derived to ensure stability. For an unstructured mesh, it is rather difficult to derive a simple equation to decide whether a scheme is (1) unconditionally unstable, (2) conditionally stable or (3) unconditionally stable. However, as the present method uses a second-order unpwind method, this almost rules out (1). A practical way to verify this hypothesis is to reduce the time step systematically until the results have converged. Based on this principle, it is found that $\Delta t = 1.0 \times 10^{-3}$ is sufficiently small for these three cases.

To achieve the accuracy given above, the CPU requirement on a 2.80 GHz computer for each time step at $h = 0.1$. $h = 0.05$ and 0.025 are 0.473, 1.176 and 3.720 s, respectively. The detailed results at $t = 100$ are provided. The drag coefficient, C_D, the recirculation length of Föppl vortices, L/D, and the separation angle, θ_s, are given in Table III together with those in previous publications for comparison. The table shows that the results have converged quite well and they are in good agreement with published data. Figure 11 shows the streamlines. The symmetric recirculation
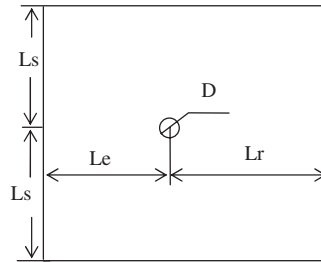
Figure 9. Computational configuration for flow past a cylinder.

Table II. Grid convergence test for flow past a cylinder at $Re=40.0$.

Case	Number of cells	Number of nodes	Number of nodes on the cylinder
1, $h=0.100$	5411	2760	29
2, $h=0.050$	7495	3816	57
3, $h=0.025$	10369	5277	105
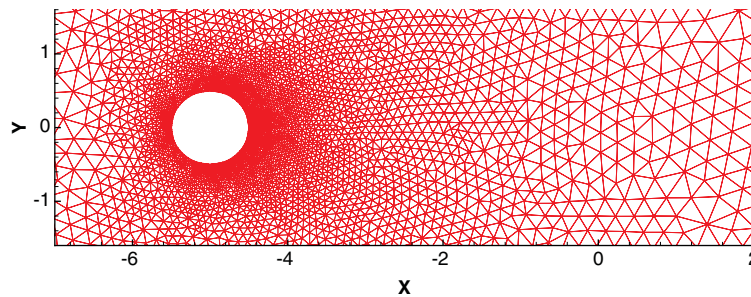
Figure 10. Grid around the cylinder.

Table III. Comparison for flow past a cylinder at $Re=40.0$.

$Re=40.0$		C_D	L/D	θ_s
Case	1	1.56	2.20	128.8°
	2	1.55	2.30	126.4°
	3	1.55	2.30	126.4°
Published data		1.52 [14]	2.26 [5]	126.4° [5]
		1.52 [15]	2.52 [16]	126.3° [16]
			2.16 [17]	126.2° [17]
				126.2° [14]

that exists behind the cylinder at this Reynolds number can be clearly seen. Figure 12 shows the pressure contours.
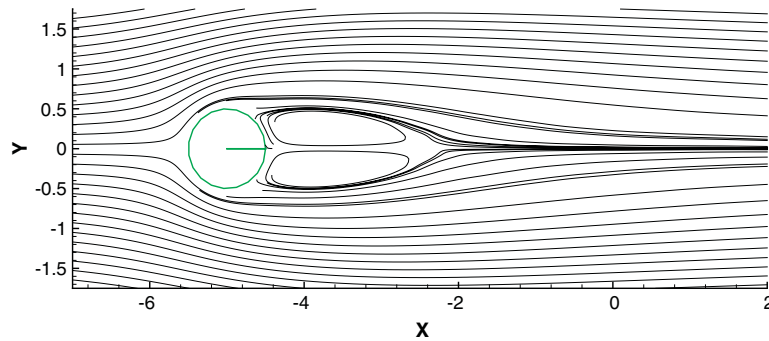
Figure 11. Streamlines for flow past a cylinder at $Re=40.0$.
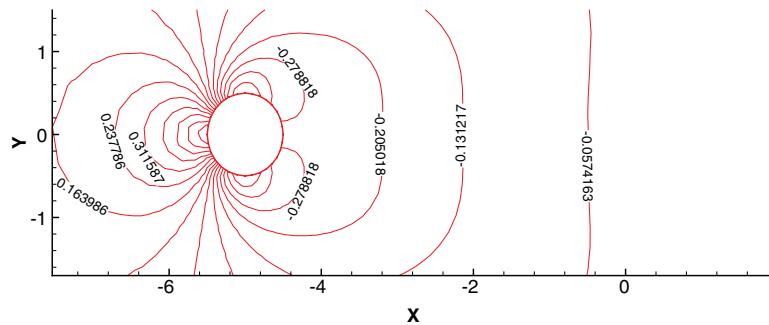
Figure 12. Pressure contours for flow past a cylinder at $Re=40.0$.

It is known that it is more difficult to obtain accurate local results such as pressure distribution than the global result such as drag or lift. To demonstrate the accuracy of the present formulation, Figure 13 gives the pressure distribution over the cylinder surface, in which the reference pressure is taken as $p=0$ at the outlet. There is some small visible difference between the results from mesh 1 and those from mesh 2. However, the results from meshes 2 and 3 are graphically identical. This once again shows the accuracy of the present formulation.

4.3. Flow in a collapsible channel

Flow in a collapsible channel or tube has many practical applications, especially in bio-medical flows. In a series of publications, Luo and Pedley [7–10] made detailed analysis for this case, including the dynamic response of the collapsible segment. Here we shall reconsider the case to further test the methodology and will also run simulations with smaller gaps. The computational configuration is shown in Figure 14. The channel away from the collapsible section has a width $D=1.0$. The section with varying width shown in the figure is part of a circle with origin at O and with radius $R=(L^2/4+c^2)/(2c)$. The flow at inlet is prescribed with $u=0.0625y(1-y)Re$ and $v=0$. The Neumann condition $\partial u/\partial x=\partial v/\partial x=0$ is imposed at the outlet and no-slip condition is applied on the wall of the channel. The reference pressure is taken from the outlet where $p=0$ is assumed. Simulations are made for cases with $c/D=0.4$ and 0.6 shown in Figure 15.
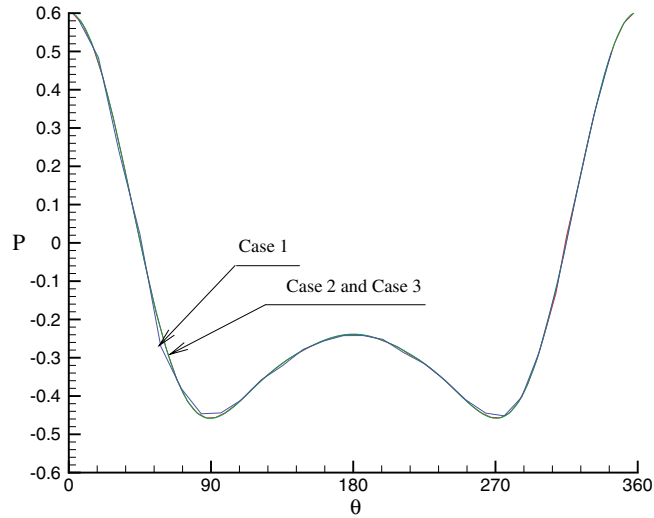
Figure 13. Pressure distribution around the cylinder at $Re=40.0$.
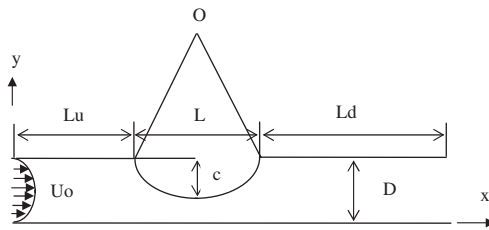

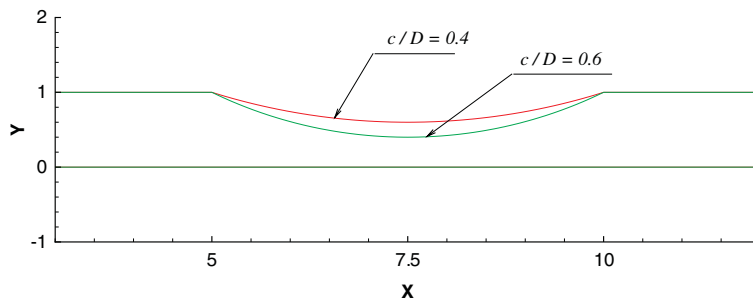Figure 14. Computational configuration for a collapsible channel.

Figure 15. The schematic diagram of the collapsible segment for two cases.

Grid convergence is first carried for the case of $c/D=0.4$ with $L_u=5.0$, $L=5.0$ and $L_d=7.0$ at $Re=300.0$. The meshes near the collapsible segment and with elements corresponding to
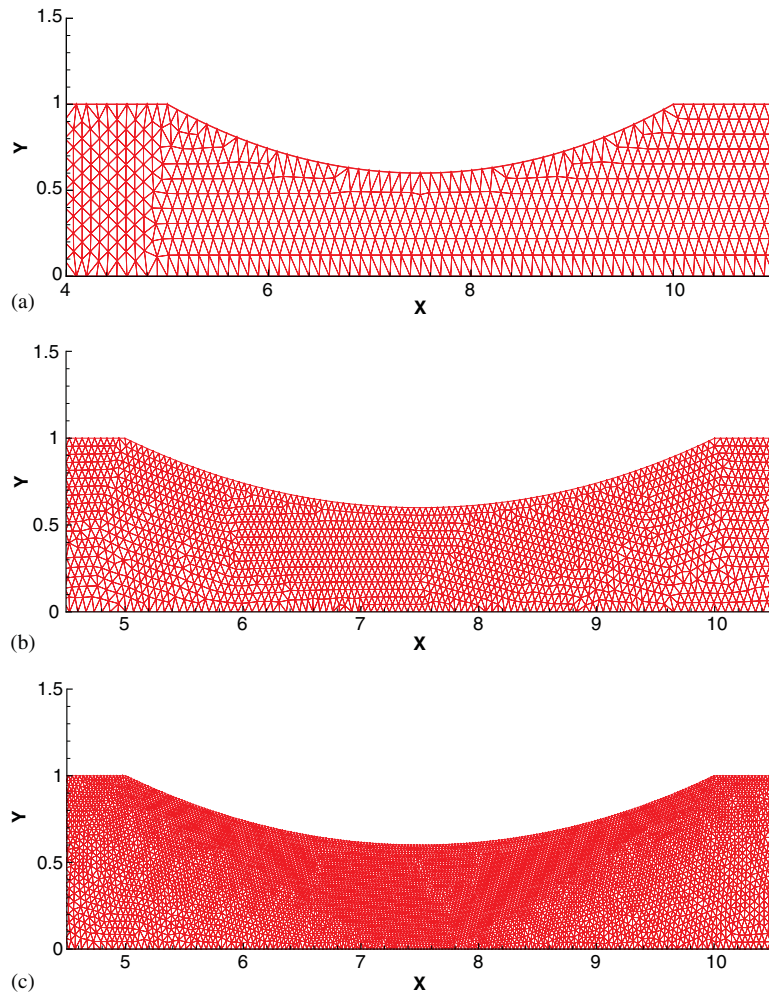
Figure 16. The grid details of collapsible segment for grid convergence test
at $c/D = 0.4$ and $L_d = 7.0$ at $Re = 300.0$.

$h = 0.1, 0.05, 0.025$ are shown in Figure 16(a)–(c), respectively. Table IV gives the comparison for the force coefficients F_x and F_y on the collapsible segments at $t = 50$. It shows that the grid with $h = 0.05$ provides results of sufficient accuracy in terms of forces, which is used in the subsequent simulations. Table V presents the results at $t = 50$ with $L_d = 30$, whereas other parameters remain the same as those of case 2 in Table IV. These two tables show that F_x is hardly affected by the length of L_d while F_y is very much different. This is because to drive the flow forward in these two cases the pressure gradient along the x direction is more or less the same, on which F_x depends. Thus, it remains almost unchanged. For F_y it depends on the value of the pressure and not the gradient in this configuration. Since the reference pressure $p = 0$ is given at the outlet, the pressure near the collapsible segment will be higher when the channel is longer. As a result F_y

is bigger. The velocity profile for u at different sections of the channel are given in Figures 17 and 18 for $L_d = 7.0$ and 30.0, respectively. For steady flow, it is expected that flow will return to the parabolic distribution as that at the inlet when the section is far away from the collapsible segment. Figures 17 and 18 have clearly showed that trend. However, $L_d = 7.0$ does not seem to be long enough for the flow at outlet to return to that at the inlet completely. When $L_d = 30.0$, the difference between the velocity profiles at the inlet and outlet is much smaller. We also plot the velocity profiles at the same sections from results corresponding to $L_d = 7.0$ and 30.0 in Figure 19. The figure shows that the length of the downstream channel does not affect the velocity profile significantly.

Further simulation is made for the case of $c/D = 0.6$ with $L_d = 30.0$. Figure 20 shows the velocity profiles at the different sections of the channel at $t = 50$. As expected, the maximum velocity beneath the collapsible section is much bigger than that corresponding to $c/D = 0.4$ because of the smaller gap between walls in this case. More detailed comparison between these two cases at $x = 7.5, 10$ is given in Figures 21 and 22. Figure 20 also shows that the reverse flow occurs at many sections. The flow at the outlet is different from that at inlet and is not even symmetrical. All these are because the flow at $c/D = 0.4$ is steady while that at $c/D = 0.6$ is unsteady. This can be more clearly seen in Figures 23 and 24 for the streamlines. Apart from a confined zone near the corner of the collapsible segment, the flow corresponding to $c/D = 0.4$ at

Table IV. Grid convergence test for flow in a collapsible channel with $L_d = 7.0$ at $Re = 300.0$.

Case	Number of cells	Number of nodes	Number of nodes on the collapsible part	F_x	F_y
1, $h = 0.100$	3332	1847	50	6.75	−13.86
2, $h = 0.050$	7576	4051	102	7.23	−14.07
3, $h = 0.025$	17555	9158	204	7.20	−14.31

Table V. The drag and lift coefficients with $L_d = 30.0$ at $Re = 300.0$.

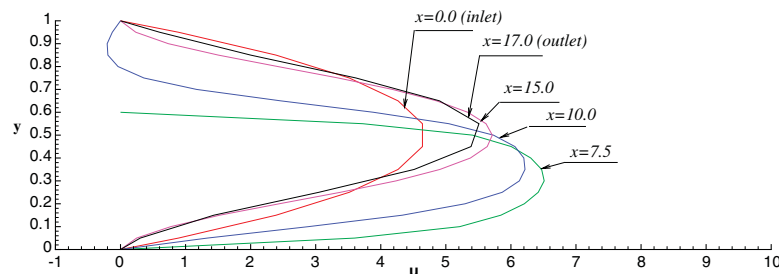| Case	Number of cells	Number of nodes	Number of nodes on the collapsible part	F_x	F_y
$h = 0.050$	17 872	9518	102	7.23	−5.35

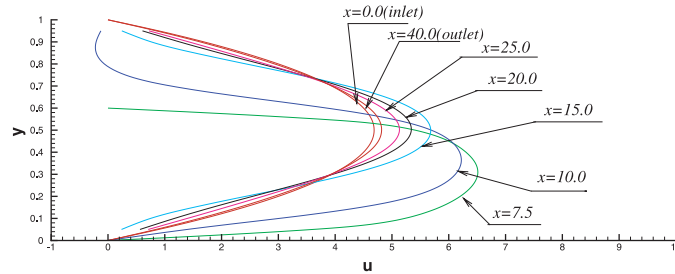Figure 17. The u-velocity profile at different x with $c/D = 0.4$, $L_d = 7.0$ and $Re = 300.0$.

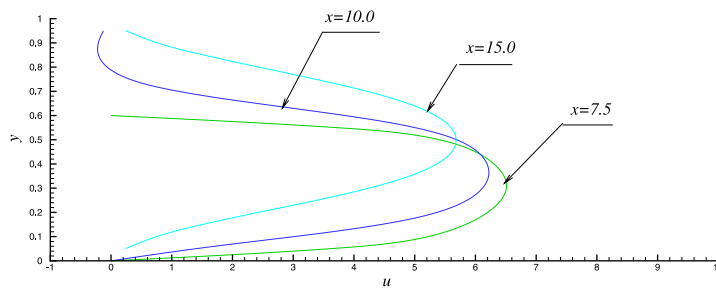Figure 18. The u-velocity profile at different x with $c/D=0.4$, $L_d=30.0$ and $Re=300.0$.

Figure 19. Comparison of the u-velocity profile at different x between $L_d=7.0$ with dashed line and $L_d=30.0$ with solid line.
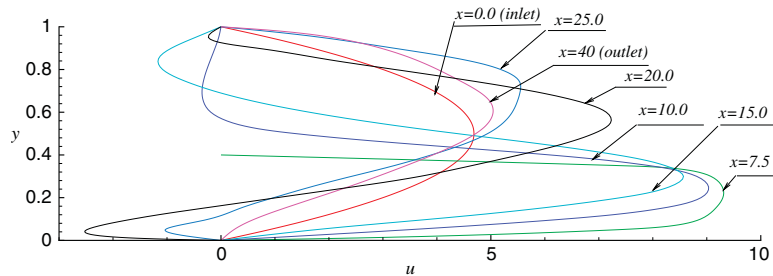

Figure 20. The u-velocity profile at different x with $c/D=0.6$, $L_d=30.0$ and $Re=300.0$.

downstream is almost uniform and steady, whereas the same flow at $c/D=0.6$ is quite unsteady. A snapshot of pressure distribution over the collapsible segment at $t=50$ is shown in Figure 25 for $c/D=0.4$ and 0.6. It shows that the maximum pressure in the latter is much bigger. The time history for force coefficients in these two cases is shown in Figures 26 and 27. Once again, the force for $c/D=0.4$ becomes steady when $t>20$, but F_y remains unsteady throughout the simulation for $c/D=0.6$. What is interesting, however, is that F_x is still more or less steady at $c/D=0.6$ even when the flow is already unsteady.
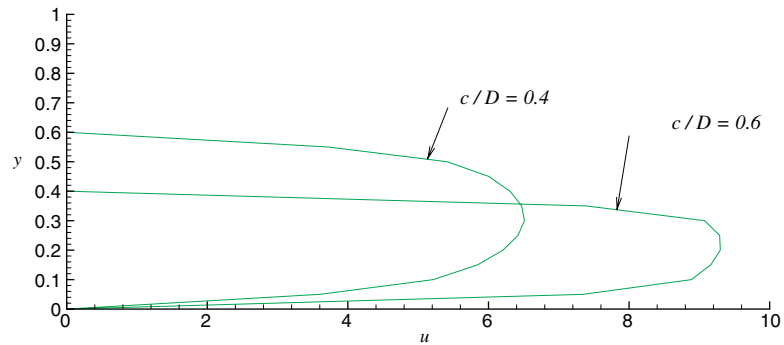
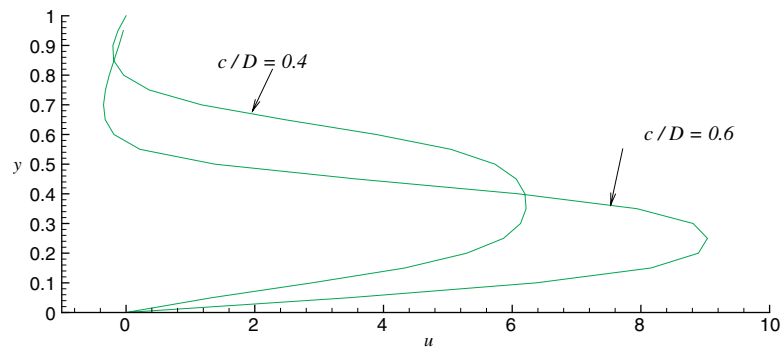Figure 21. The u-velocity profile at $x = 7.5$ with different c/D at $L_d = 30.0$ and $Re = 300.0$.

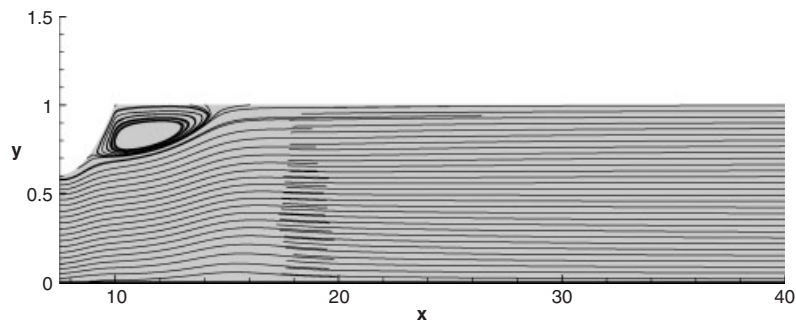Figure 22. The u-velocity profile at $x = 10.0$ with different c/D at $L_d = 30.0$ and $Re = 300.0$.

Figure 23. Streamlines for $c/D = 0.4$ at $Re = 300.0$.

5. CONCLUSIONS

A new finite volume method for the Navier–Stokes equation has been developed. In addition to the velocity and the pressure, the method has also introduced their derivatives at the cell centres.
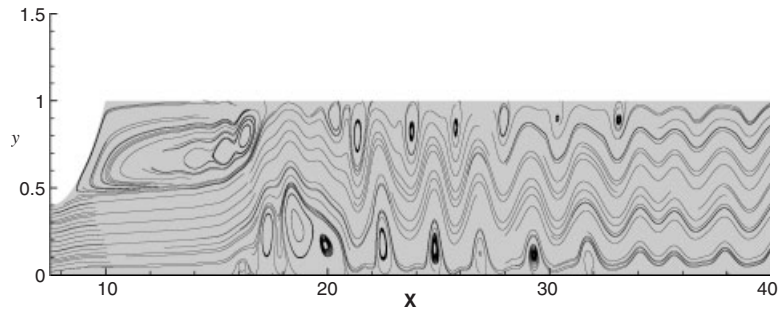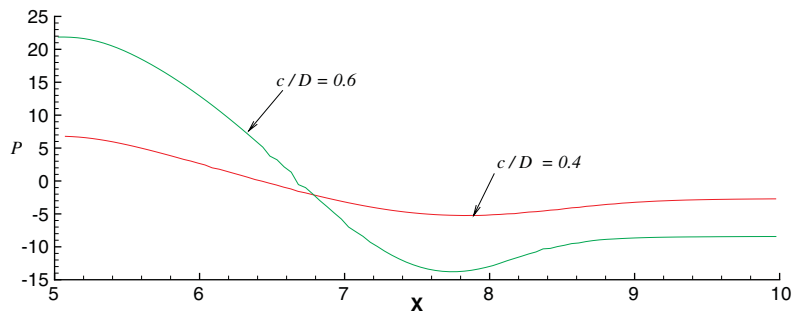
Figure 24. Streamlines for $c/D=0.6$ at $Re=300.0$.

Figure 25. The pressure distributions around the collapsible segment with
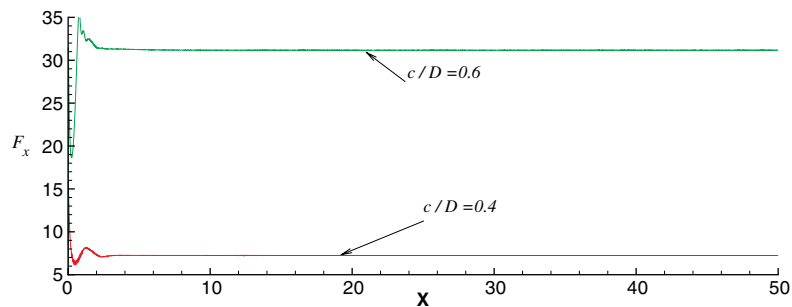different c/D at $L_d=30.0$ and $Re=300.0$.

Figure 26. The force coefficient F_x with different c/D at $L_d=30.0$ and $Re=300.0$.

As a result, the sources of error at each step have been revealed. This has allowed accurate results to be obtained as demonstrated by the test cases. The results for the collapsible channel with small gap are particularly promising. It shows that the method may be used for the case in which the
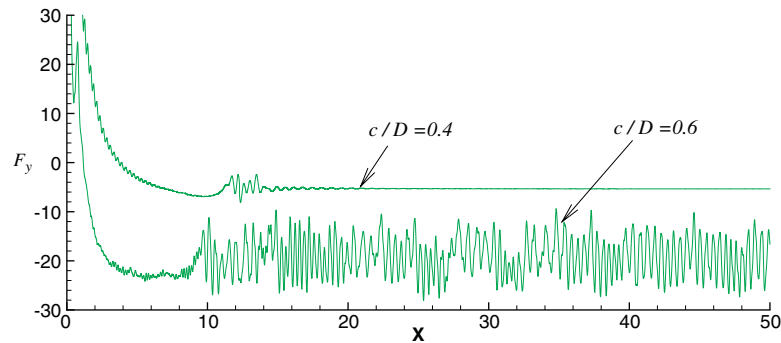
Figure 27. The force coefficient F_y with different c/D at $L_d = 30.0$ and $Re = 300.0$.

collapsible segment is in large amplitude motion. It is also evident that the present formulation can be further extended to the three-dimensional flow problem.

REFERENCES

1. Wu GX, Hu ZZ. Numerical simulation of viscous flow around unrestrained cylinders. *Journal of Fluids and Structures* 2006; **22**:371–390.
2. Ferziger JH, Peric M. *Computational Methods for Fluid Dynamics* (2nd edn). Springer: Berlin, 1999.
3. Syrakos A, Goulas A. Estimate of the truncation error of finite volume descretization of the Navier–Stokes equations on collocated grids. *International Journal for Numerical Methods in Fluids* 2006; **50**:103–130.
4. Zang Y, Street RL, Koseff JR. A non-staggered grid, fractional step method for time-dependent incompressible Navier–Stokes equations in curvilinear coordinates. *Journal of Computational Physics* 1994; **114**:18–33.
5. Hu ZZ, Greaves DM, Wu GX. Numerical simulation of fluid flows using an unstructured finite volume method with adaptive tri-tree grids. *International Journal for Numerical Methods in Fluids* 2002; **39**:403–440.
6. Lilek Ž, Peric M. A fourth-order finite volume method with collocated variable arrangement. *Computers and Fluids* 1995; **24**:239–252.
7. Luo XY, Pedley TJ. A numerical simulation of steady flow in a 2-D collapsible channel. *Journal of Fluids and Structures* 1995; **9**:149–174.
8. Luo XY, Pedley TJ. A numerical simulation of unsteady flow in a two-dimensional collapsible channel. *Journal of Fluid Mechanics* 1996; **314**:191–225.
9. Luo XY, Pedley TJ. The effects of the wall inertia on the 2-D collapsible channel flow. *Journal of Fluid Mechanics* 1998; **363**:253–280.
10. Luo XY, Pedley TJ. Multiple solutions and flow limitation in collapsible channel flows. *Journal of Fluid Mechanics* 2000; **420**:301–324.
11. Lehnhauser T, Schafer M. Improved linear interpolation practice for finite-volume schemes on complex grids. *International Journal for Numerical Methods in Fluids* 2002; **38**:625–645.
12. Patankar SV, Spalding DB. A calculation procedure for heat, mass and momentum transfer in three-dimensional parabolic flows. *International Journal of Heat and Mass Transfer* 1972; **15**:1787–1806.
13. Giraldo FX. *Mesh2D—2D Adaptive Mesh Generator*. http://www.nrlmry.navy.mil/~giraldo/mesh2d.html# ExamplesA. 1997.
14. Franke R, Rodi W, Schönung B. Numerical calculation of laminar vortex shedding flow past cylinders. *Journal of Wind Engineering and Industrial Aerodynamics* 1990; **35**:237–257.
15. Dennis SCR, Chang GZ. Numerical solution for steady flow past a circular cylinder at Reynolds numbers up to 100. *Journal of Fluid Mechanics* 1970; **42**:471–489.
16. Kawaguti M, Jain PC. Numerical study of a viscous fluid flow past a circular cylinder. *Journal of Physics Society of Japan* 1966; **21**:2055–2065.
17. Collins WM, Dennis SCR. Flow past an impulsively started circular cylinder. *Journal of Fluid Mechanics* 1973; **60**:105–127.